Available online at www.sciencedirect.com
ScienceDirect
Journal of the European Ceramic Society 32 (2012) 77–83
www.elsevier.com/locate/jeurceramsoc

Mechanical properties of Al_2O_3–Cr_2O_3/Cr_3C_2 nanocomposite fabricated by spark plasma sintering

Hao-Tung Lin [a], Pramoda K. Nayak [b], Bo-Zon Liu [b], Wei-Hsio Chen [b], Jow-Lay Huang [b,c,d,*]

[a] Electrical Technology Center, Cheng Shiu University, Kaohsiung County 833, Taiwan
[b] Department of Materials Science and Engineering, National Cheng-Kung University, Tainan 701, Taiwan
[c] Center for Micro/Nano Science and Technology, National Cheng Kung University, Tainan 701, Taiwan
[d] Research Center for Energy Technology and Strategy, National Cheng Kung University, Tainan 701, Taiwan

Received 7 March 2011; received in revised form 19 July 2011; accepted 23 July 2011

Abstract

The fine grains of Al_2O_3–Cr_2O_3/Cr-carbide nanocomposites were prepared by employing recently developed spark plasma sintering (SPS) technique. The initial materials were fabricated by a metal organic chemical vapor deposition (MOCVD) process, in which $Cr(CO)_6$ was used as a precursor and Al_2O_3 powders as matrix in a spouted chamber. The basic mechanical properties like hardness, fracture strength and toughness, and the nanoindentation characterization of nanocomposites such as Elastics modulus (E), elastic work (W_e) and plastic work (W_p) were analyzed. The microstructure of dislocation, transgranular and step-wise fracture surface were observed in the nanocomposites. The nanocomposites show fracture toughness of (4.8 MPa $m^{1/2}$) and facture strength (780 MPa), which is higher than monolithic alumina. The strengthening mechanism from the secondary phase and solid solution are also discussed in the present work. Nanoindentation characterization further illustrates the strengthening of nanocomposites.

Keywords: Al_2O_3; Spark plasma sintering; Nanocomposites; Mechanical properties; Nanoindentation

1. Introduction

The Cr_3C_2 is a good reinforcement material for Al_2O_3 due to its high melting point, high hardness, high Young's modulus and wear resistance.[1–3] It is also a material with high electrical conductivity and the Cr_3C_2/Al_2O_3 composite has potential applications for electrical discharge machining (EDM).[4] Chromia (Cr_2O_3) has been used to improve the physical properties of Al_2O_3.[5–9] As Cr_2O_3 has the same corundum crystal structure similar to Al_2O_3, Al_2O_3–Cr_2O_3 can form substitutional solid solution in all ranges at high temperature. The addition of Cr_2O_3 was found to increase the hardness, tensile strength, and thermal shock resistance of Al_2O_3.

It has been found that the combination of conventional fluidized bed technology with chemical vapor deposition (CVD) is an effective method to deposit particles. Several researchers have reported the coating of secondary phase particles on the ceramic matrix material using MOCVD process in a fluidized bed.[10–13] In previous study,[14] Al_2O_3/Cr-species composites have been prepared by using $Cr(CO)_6$ as the precursor of MOCVD and using alumina as the fluidizing matrix materials. The results indicate that besides Cr_2O_3, the decomposed $Cr(CO)_6$ contains free carbon. When the spouted powders were used as the initial powder in the spark plasma sintering (SPS) process, some Cr_2O_3 reacted with Al_2O_3 to form Al_2O_3–Cr_2O_3 solid solution and some Cr_2O_3 reacted with carbon to form Cr_3C_2. The Cr_3C_2 inhibited Al_2O_3 gain growth and the fine grain sized Al_2O_3–Cr_2O_3/Cr-carbide nanocomposites were fabricated as reported before.[15]

The nanoindentation test has been established as an important tool for the mechanical characterization of materials on the submicron scale.[16,17] According to the reports of Oliver and Pharr,[18,19] such a test is usually conducted using instrumented

* Corresponding author at: Department of Materials Science and Engineering, National Cheng-Kung University, Tainan 701, Taiwan. Tel.: +886 6234 8188; fax: +886 6276 3586.
E-mail address: JLH888@mail.ncku.edu.tw (J.-L. Huang).

0955-2219/$ – see front matter © 2011 Elsevier Ltd. All rights reserved.
doi:10.1016/j.jeurceramsoc.2011.07.029

machines in which indenter load (P), and indenter displacement (h), can be continuously and simultaneously recorded during indenter loading and unloading. The unloading data are then analyzed to yield the hardness (H), and the Young's modulus (E). The loading curve is considered to follow Kick's law[20]

$$P = Ch^2 \tag{1}$$

where P is the indenter load and h is the elastic displacement (penetration depth) of the indenter. C is a constant that depends on elastic and plastic materials properties, as well as indenter geometry. The total work done by loading (W_t) and the elastic work done by the elastic unloading (W_e) are calculated from the areas underneath the loading and unloading curves, respectively.[21] The plastic work done (W_p) by the indentation process is the area enclosed by loading and unloading curve, i.e.,

$$W_p = W_t - W_e \tag{2}$$

Elastic modulus of the test material can be calculated from the loading–unloading curves of the load (P) as a function of the displacement (h), given by

$$E_r = \frac{\sqrt{\pi}}{2\beta\sqrt{A_c}} \times \left.\frac{dp}{dh}\right|_{h_{\max}} \tag{3}$$

where E_r is the reduced Young's modulus, $h_{\max}$ is the maximum penetration depth, A_c is the projected contact area measured at $h_{\max}$ and β is a constant equal to 1.034 for a Berkovich indenter. The reduced Young's modulus (E_r) is given through the equation,

$$\frac{1}{E_r} = \frac{1-\upsilon^2}{E} + \frac{1-\upsilon_i^2}{E_i} \tag{4}$$

where υ and υ_i (0.07) are Poisson ratio of the material and indenter, respectively, and E_i (1141 GPa) is Young's modulus of the indenter. The Young's modulus (E) can be calculated from Eqs. (3) and (4), which is given by,

$$E = (1-\upsilon^2)\left[\frac{2\sqrt{A_c}}{S\sqrt{\pi}} - \frac{(1-\upsilon_i^2)}{E_i}\right]^{-1} \tag{5}$$

$$S = \left.\frac{dp}{dh}\right|_{h_{\max}} \tag{6}$$

where S is the unloading stiffness measured at the maximum penetration displacement.

In the present study, the initial nanocomposite powders consisting of nanosized Cr_2O_3 particles coated on Al_2O_3 powders have been fabricated by a metal organic chemical vapor deposition (MOCVD), in which $Cr(CO)_6$ was used as a precursor and Al_2O_3 powders as matrix in a spouted chamber. Then, the fine grains of Al_2O_3–Cr_2O_3/Cr-carbide nanocomposites were prepared by employing recently developed spark plasma sintering (SPS) technique. The basic mechanical properties such as density, fracture strength, and toughness measured of Al_2O_3–Cr_2O_3/Cr_3C_2 nanocomposites have been measured. Besides, the nanoindentation characterizations of these composites are also discussed in this work.

2. Experimental details

2.1. Powder and sample preparation

α-Alumina (Al_2O_3, 99.99%, Taimei Chemicals Co. Ltd., Japan) with grain size about 150 nm was used as the matrix material in this study. Chromium hexacarbonyl ($Cr(CO)_6$, 99%, Strem Chemicals Co., USA) was used as the precursor of chromium oxide in a MOCVD process. $Cr(CO)_6$ was initially heated for evaporation at 75 °C and He gas was inserted as the carrier gas for transporting these precursor vapors, into the reaction chamber in a spouted bed. The nanosized composite powders fabricated in the spouted bed for 30 and 60 min were named as S-30 and S-60, respectively. The pressure of reaction chamber was controlled at 10 Torr, and the reaction temperature was kept at 300 °C.

2.2. Densification

The as spouted powders were densified by using SPS process (SPS-515S, Shumitomo, Japan). 1.5 g of powder (monolithic Al_2O_3, S-30, S-60) was put into a graphite mold of 15.5 mm diameter. The uniaxial pressure of 50 MPa was imposed on the powder and the vacuum level was less than 6 Pa. The samples were heated with a heating rate of 200 °C/min from room temperature to 600 °C and then with 100 °C/min from 600 °C to 1350 °C. The holding time at the sintering temperature, 1350 °C was kept for 10 min.

2.3. Density, fracture strength and toughness

The density was calculated according the Archimedes principle. The fracture strength was determined by 3-point bending (Shimadzu AG-IS 100KN, Japan) method. The toughness was measured by single-edge-precracked beam (SEPB). A precrack with depth of 0.254 mm was conducted in the center of sample by a diamond cutter with a thickness of 0.15 mm. The density, fracture strength and toughness reported in this work are the average of five testing results.

2.4. Microstructure

The microstructures and composition of the specimens were characterized by field emission gun scanning transmission electron microscopy (FEG-STEM, FEI Tecnai G2 F20, Netherlands) and field emission scanning electron microscope (FESEM, PHILIPS XL40, Netherlands). The content of Al and Cr was analyzed by X-ray Fluorescence (XRF, Rigaku Rix2000, Japan).

2.5. Nanoindentation test

For the nanoindentation tests, the surfaces of the samples were mechanically polished using diamond paste down to 1 μm. Displacement-sensing indentation tests were performed using a nanoindentation by Universal Nanomechanical Tester (UNAT, ASMEC GmbH, Germany) with a diamond Berkovich indenter. Five peak loads (300 mN, 600 mN, 900 mN, 1200 mN and

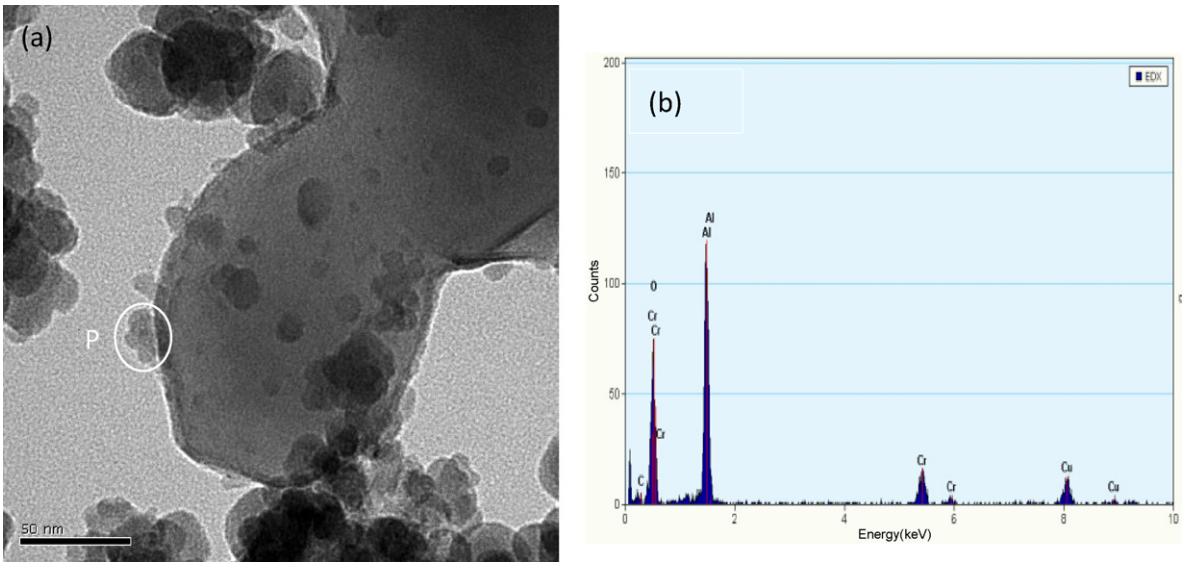

Fig. 1. TEM micrographs of (a) nanoparticles deposited on alumina particle and (b) EDS spectrum of the coating particle.

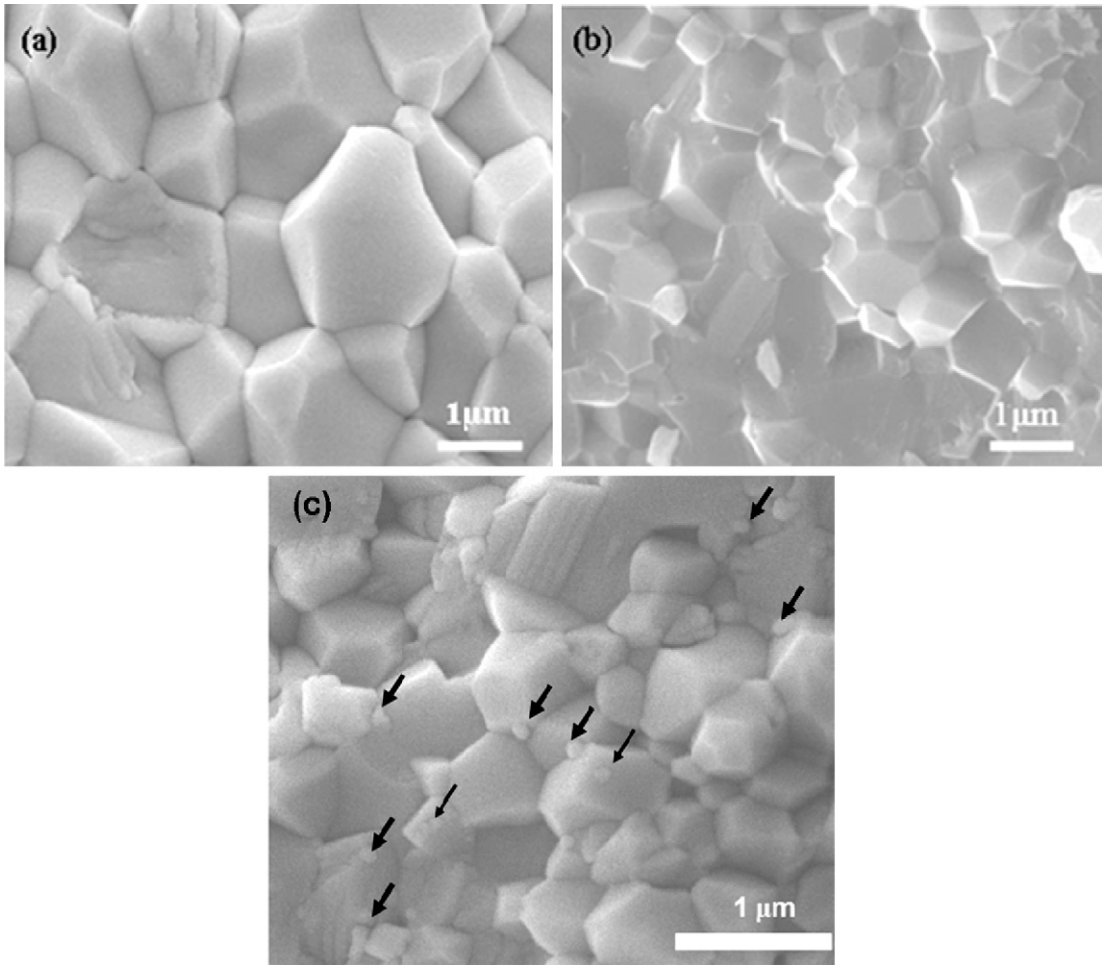

Fig. 2. SEM micrographs of fracture surface of 1350 °C fully dense SPS specimen of (a) Al_2O_3, (b) S-30, and (c) S-60.

Table 1
The content of Al and Cr of 300 °C fluidized bed powder from XRF analysis.

Fluidized powder	Al (wt.%)	Cr (wt.%)	Others (C & O) (wt.%)
Fluidized for 30 min	58.75	2.72	38.53
Fluidized for 60 min	57.33	4.98	37.78

1500 mN) were used to investigate the elastic modulus (E), plastic work (W_p) and elastic work (W_e) of the nanocomposites. The indenter achieved the peak load within 10 s and kept for 5 s hold time at the peak load. For each peak load, at least 10 indentations, spaced at 40 μm, were made. Elastic modulus (E), plastic work (W_p) and elastic work (W_e) were calculated by means of the nanoindenter software Inspector X (produced by the ASMEC GmbH), based on the model of Oliver and Pharr.[18,19]

3. Results and discussion

3.1. Fracture strength and toughness

The compositions of the decomposed precursor $Cr(CO)_6$ include Cr_2O_3 and carbon (C) analyzed by XPS in our previous study.[14] Fig. 1 shows the nanosized chromium oxide (Cr_2O_3) particles coated on alumina (Al_2O_3) matrix powder. The content of Al and Cr has been calculated from the XRF analysis and shown in Table 1. It is observed that the Cr content in S-60 spouted powders was 4.98 wt.%, higher than that in S-30 (2.72 wt.%).

The pure alumina powder and initial powder of S-30 and S-60 were densified by spark plasma sintering at 1350 °C for 10 min. During sintering, the solid solution of Al_2O_3–Cr_2O_3 and secondary phase of carbide, Cr_3C_2 particles were formed in the matrix of nanocomposites due to the reaction between Cr_2O_3 and Al_2O_3, and between Cr_2O_3 and C. From the TEM diffraction pattern illustrated in our previous report,[15] it is clear that the secondary phase is Cr_3C_2. The density and porosity of pure alumina bulk and S-30 and S-60 nanocomposites are listed in Table 2. The density of pure alumina is found to be 99.25%, and due to uncertain amount of carbide and solid solution in the alumina matrix, the relative density of nanocoposites were not calculated accurately. But the low apparent porosity of S-30 (0.3%) and S-60 (0.1%) indicates that almost fully dense S-30 and S-60 nanocomposites were fabricated by SPS. The fracture surfaces of the nanocomposites are shown in Fig. 2. It indicates that the pure alumina exhibits larger grain size (~1.5 μm) than that of S-30 (~1.0 μm) and S-60 (~0.6 μm) densification samples. The nanosized reinforced particles (Cr_3C_2) about 100 nm

Table 2
Density and porosity of pure alumina and S-30 and S-60 nanocomposites.

Bulk	Apparent density (g/cm^3)	Relative density (%)
Al_2O_3	3.95	99.25
	Apparent density (g/cm^3)	Apparent porosity (%)
S-30	4.07	0.3
S-60	4.1	0.1

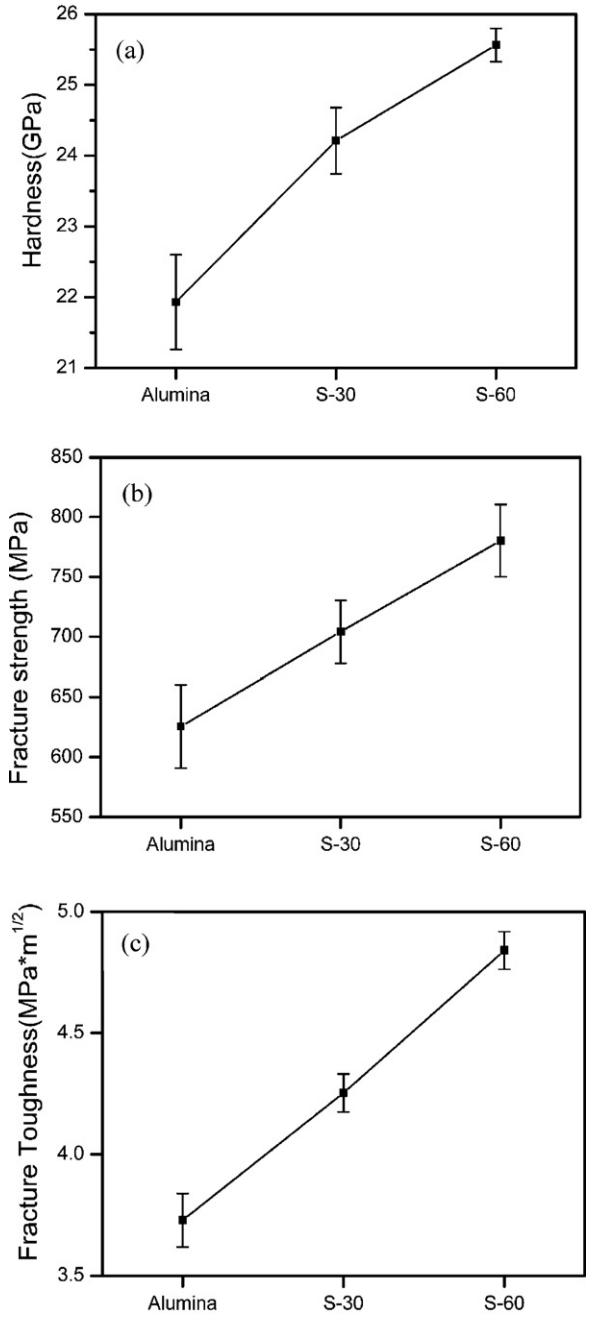

Fig. 3. (a) Hardness, (b) fracture strength, and (c) toughness of alumina and Al_2O_3–Cr_2O_3/Cr_3C_2 nanocomposite.

are found in the intergranular and intragranular locations, as shown by thick and thin arrows in Fig. 2(c), respectively. S-60 densification sample has smallest grain size due the more amounts of secondary phase particles to inhibit its grain growth. The hardness, fracture strength and toughness of the S-30 and S-60 nanocomposites are shown in Fig. 3. From this figure, we can see that the S-60 nanocomposite exhibits highest fracture strength and toughness.

3.1.1. Secondary particles strengthening

Nanocomposites consist of nano-particles dispersed within matrix grains and intergrains. The fracture mode changes from

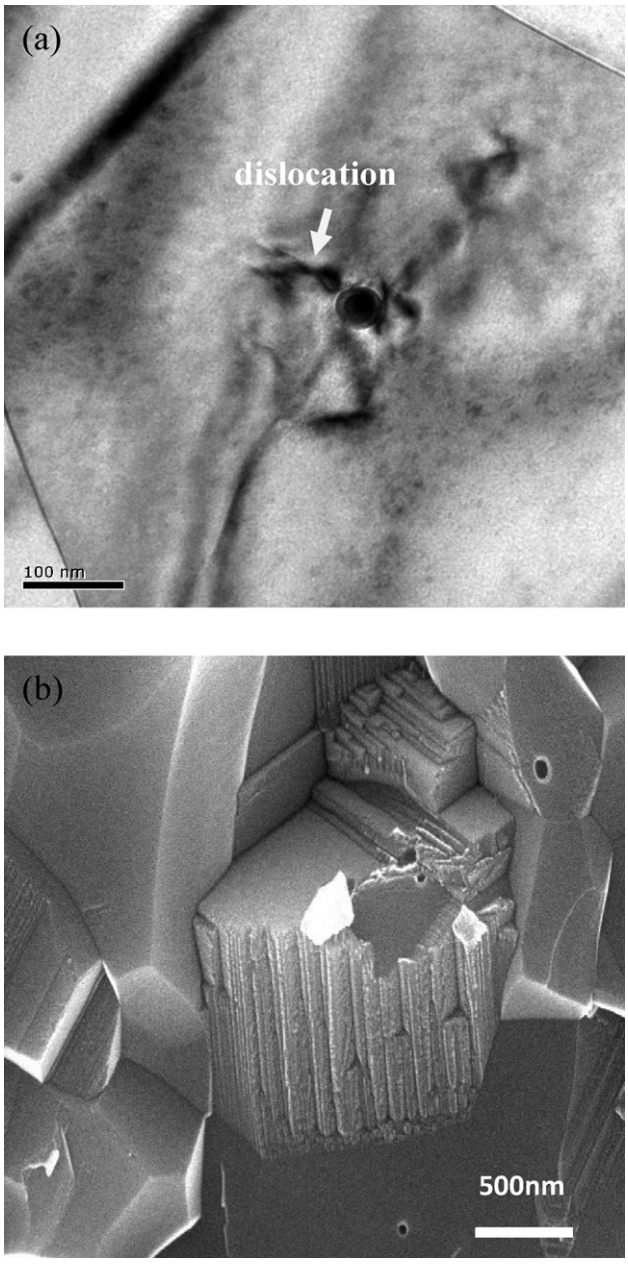

Fig. 4. (a) TEM micrograph and (b) SEM micrograph of the step fracture surface of Al_2O_3–Cr_2O_3/Cr-carbide nanocomposite.

that of the intergranular fracture in monolithic alumina to that of the mixture of intergranular and transgranular fracture in nanocomposites, as shown in Fig. 2. These nanocomposites result in the generation of thermally induced residual stresses after sintering. The mismatch in thermal expansion coefficient (TEC) between the matrix (α-$Al_2O_3 = 8.4 \times 10^{-6}/^{\circ}C$), and the dispersed particles ($Cr_3C_2 = 11.2 \times 10^{-6}/^{\circ}C$) yields highly localized residual stresses around the particles. Due to higher TEC of the Cr-carbide particles, the compress stress would be induced in the alumina matrix and increase the strength. This is different than that of secondary particles SiC, which results in tensile stress in alumina matrix.[22] The stress around the Cr-carbide induces the formation of dislocation in alumina matrix, as shown in Fig. 4(a). The crack propagation path changes when it becomes closer to the Cr-carbide particles. The step-wise fracture surface rather than a planar cleavage plane is observed in the nanocomposites, as shown in Fig. 4(b). Similar result was reported by Choi et al.,[23,24] who indicated that the nanocracking around the dislocation resulted in the step-wise fracture surface. Hence, it is assumed that the reinforcement of the Cr_3C_2 particles, small grain size of Al_2O_3 matrix and the compress residual stresses in the matrix grains result in improvement of the strength of nanocomposites.

Table 3
Contact displacement (μm) of monolithic Al_2O_3, and Al_2O_3–Cr_2O_3/Cr-carbide nanocomposites sintered at 1350 °C under various indentation loading.

Bulk	300 mN	600 mN	900 mN	1200 mN	1500 mN
Al_2O_3	0.649	1.058	1.220	1.517	1.730
S-30	0.644	1.003	1.204	1.478	1.664
S-60	0.638	0.993	1.133	1.432	1.594

3.1.2. Solid solution strengthening

The formation of chromium (III) oxide solid solution in aluminium (III) oxide was confirmed by X-ray diffraction observations, reported in our previous paper.[14] The Cr^{3+} ions increase the growth rate of Al_2O_3 grain because of the coherency strain energy at grain boundary.[25–27] However, this phenomenon is not found in the nanocomposites. It is attributed that the secondary particles of Cr_3C_2 inhibits the growth of alumina matrix. The fracture strength is increased by the grain-boundary modification caused the compressive stress generated by the substitution of bigger ion Cr^{3+} ion (0.076 nm) in place of smaller Al^{3+} ion (0.068 nm). The localized compressive stress helps in strengthening the grain boundary, and then the fracture strength increases by this effect.[28]

3.2. Nanoindentation

Typical indentation load–displacement hysteresis loops under indentation loads (P_{max} = 300, 600, 900, 1200, 1500 mN) registered for the monolithic alumina and Al_2O_3–Cr_2O_3/Cr_3C_2 nanocomposites are depicted in Fig. 5. Under the same peak load, the indentation displacement of the monolithic alumina is larger than that of the Al_2O_3–Cr_2O_3/Cr_3C_2 nanocomposites. This observation implies that the hardness increases in the Al_2O_3–Cr_2O_3/Cr_3C_2 nanocomposites and it is consistent with the results shown in Fig. 3(a).

Fig. 5(a) shows that a larger displacement difference between 300 mN and 600 mN is found compared to the difference between 600 mN and 900 mN, 900 mN and 1200 mN, 1200 mN and 1500 mN. The numerical data of the displacement of monolithic Al_2O_3, and Al_2O_3–Cr_2O_3/Cr-carbide nanocomposites under various peak loads are listed in Table 3. The plastic work (W_p) done by the indentation process is the area enclosed by loading and unloading curve. For monolithic alumina, it is suggested that the significant plastic formation already happened at the peak load of 600 mN. When the 600 mN peak load conducted on the monolithic alumina, the corresponding value of plastic work (W_p) 155.9 nJ was calculated. Consid-

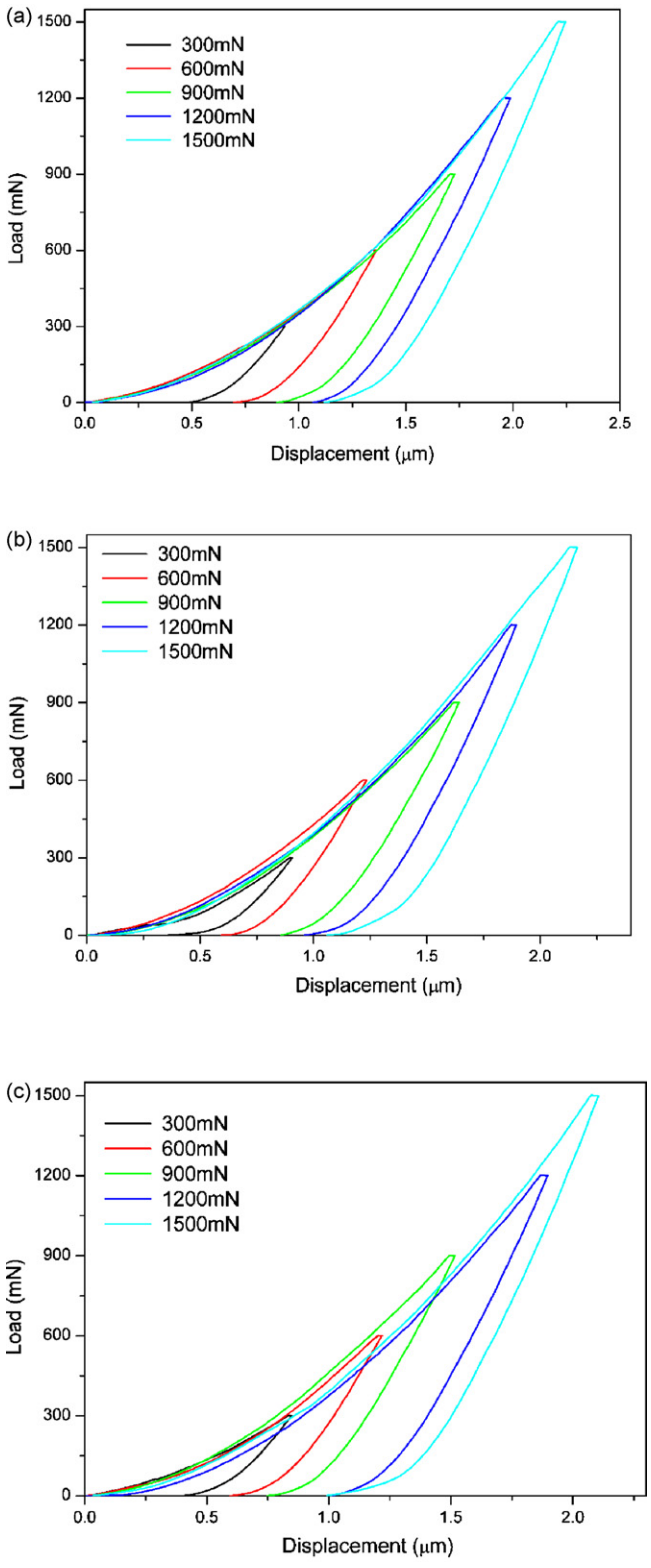

Fig. 5. The load–displacement curves of (a) monolithic Al_2O_3, (b) S-30, and (c) S-60 with the load from 300 mN to 1500 mN followed by SPS sintered at 1350 °C.

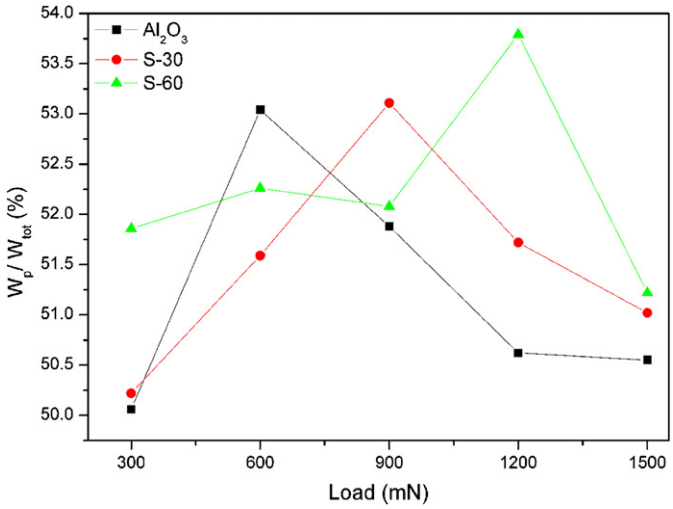

Fig. 6. W_p/W_{tot} of Al_2O_3 and Cr_3C_2/Al_2O_3 nanocomposites at 1350 °C with the load from 300 mN to 1500 mN.

ering the nanocomposites of S-30 and S-60, Fig. 5(b) shows the larger displacement difference happens between 600 mN and 900 mN. Fig. 5(c) indicates larger displacement difference between 900 mN and 1200 mN. The value of plastic work (W_p) done in S-30 nanocomposite at the peak load of 900 mN was 265.5 nJ and the plastic work (W_p) done in S-60 nanocomposite at the peak load of 1200 mN was 412.2 nJ. These results indicate that nanocomposites are able to endure higher plastic deformation than monolithic alumina. Consistent results are found in Fig. 6, which shows that the W_p/W_{tot} ratio of Al_2O_3, S-30 and S-60 is the function of peak load and the largest value of W_p/W_{tot} ratio is at 600 mN, 900 mN and 1200 mN, respectively.

The elastic modulus of monolithic Al_2O_3, S-30 and S-60 nanocomposites can be measured from the slope of unloading curves. Fig. 7 shows that in all three samples, the elastic modulus decreases with the increase of peak load. The significantly decrease in elastic modulus for monolithic happened between 300 mN and 600 mN and for S-30 nanocomposite, that

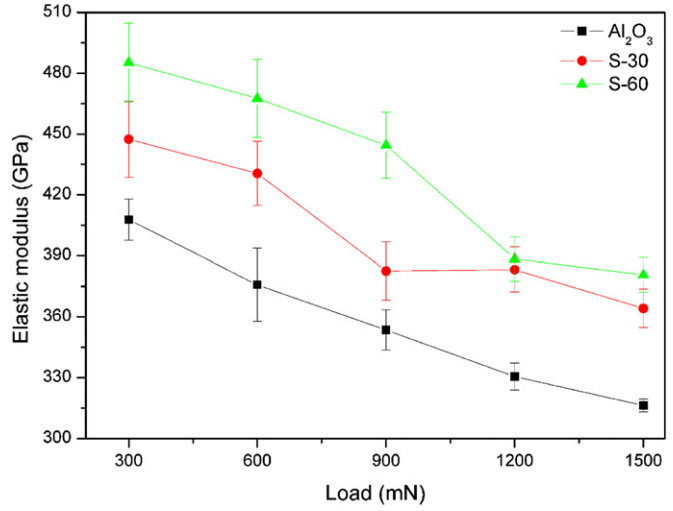

Fig. 7. The elastic modulus of Al_2O_3 and Cr_3C_2/Al_2O_3 nanocomposites sintered at 1350 °C for 10 min by SPS with the load from 300 mN to 1500 mN.

is happened between 600 mN and 900 mN. Similarly, for S-60 nanocomposite, the elastic modulus decreases significantly between 900 mN and 1200 mN. This result is consistent with the results shown in Figs. 5 and 6.

Guicciardi et al.[29] indicated that when the contact displacement is smaller than its mean grain size, due to the indentation size effect (ISE)[30] a larger elastic modulus would be measured. It mainly reflects the response of the Al_2O_3 single phase. While highly distorted atomic bonds, those found at the grain boundaries are to have lower elastic modulus than the undistorted bonds. In order to present the effect of size effect, the displacement should be equal to or larger than the mean grain size. By increasing the peak load, the contact depth becomes deeper and elastic modulus tends to decrease gradually. In all three samples, the data dispersion reduces with the increasing peak load. Nanocomposites of S-30 and S-60 have higher elastic modulus than that of monolithic alumina. It is attributed to the secondary phase of Cr_3C_2 with a higher elastic modulus and the formation of solid solution, in which the larger Cr^{3+} ion replaces Al^{3+} to induce compressive stress in the grain boundary. Therefore, the nanoindentation characterization of nanocomposites further illustrates the strengthening of mechanical properties.

4. Conclusions

A comparison with monolithic alumina, the Al_2O_3–Cr_2O_3/Cr_3C_2 nanocomposites exhibit higher hardness, fracture strength and toughness due to the strengthening of secondary phase of Cr_3C_2 particles and solid solution of Al_2O_3–Cr_2O_3. Small grain size of Al_2O_3 matrix, transgranular fracture, and step-wise fracture surface are observed in nanocomposites. Nanoindentation characteristic further illustrates the strengthening of nanocomposites, which shows that nanocomposites have higher plastic deformation and endure higher plastic work and elastic modulus than that of monolithic alumina.

Acknowledgements

The authors thanks to the National Science Council of the ROC for its financial support under the contract no. NSC 99-2923-E-006-002-MY3. The authors would like to thank Dr. Yang-Yuan Chen of Institute of Physics, Academia Sinica, Taipei, Taiwan, ROC to carry out SPS measurements.

References

1. Lii DF, Huang JL, Huang JJ, Lu HH. The interfacial reaction in Cr_3C_2/Al_2O_3 composites. *J Mater Res* 1999;**14**:817–23.
2. Huang JL, Lin HD, Jeng CA, Lii DF. Crack growth resistance of Cr_3C_2/Al_2O_3 composites. *Mater Sci Eng A* 2000;**279**:81–6.
3. Huang JL, Twu KC, Lii DF, Li AK. Investigation of Al_2O_3/Cr_3C_2 composites prepared by pressure less sintering (part 2). *Mater Chem Phys* 1997;**51**:211–5.
4. Shu KM, Fu CT, Wu JM. Electrodischarge-machining of Al_2O_3/Cr_3C_2 composites. *J Mater Sci Lett* 1994;**13**:1146–8.
5. Bradt RC. Cr_2O_3 solid solution hardening of Al_2O_3. *J Am Ceram Soc* 1967;**50**:54–5.
6. Chate BB, Smith WC, Kim CH, Hasselman DPH, Kane GE. Effect of chromia alloying on machining performance of alumina ceramic cutting tools. *Am Ceram Soc Bull* 1975;**54**:210–5.
7. Davies TJ, Emblem HG, Harabi A, Nwobodo CS, Ogwu AA, Tsantzlaou V. Characterisation and properties of alumina–chrome refractories. *Br Ceram Trans* 1992;**91**:71–6.
8. Harabi A, Davies TJ. Mechanical properties of sintered alumina chromia refractories. *Br Ceram Trans* 1995;**94**:79–84.
9. Riu DH, Kong YM, Kim HE. Effect of Cr_2O_3 addition on microstructural evolution and mechanical properties of Al_2O. *J Eur Ceram Soc* 2000;**20**:1475–81.
10. Morooka S, Kobata A, Kusakabe K. Rate analysis of composite ceramic particles production by CVD reactions in a fluidized bed. *AIChE Symp Ser* 1991;**87**:32–7.
11. Tsugeki K, Kato T, Koyanagi Y, Kusakabe K, Morooka S. Electconductivity of sintered bodies of α-Al_2O_3–TiN composite prepared by CVD reaction in a fluidized bed. *J Mater Sci* 1993;**28**:3168–72.
12. Wood BJ, Sanjurjo A, Tong GT, Swider SE. Coating particles by chemical vapor deposition in fluidized bed reactors. *Surf Coat Technol* 1991;**49**:228–32.
13. Hua B, Li C. Production and characterization of nanocrystalline SnO_2 films on Al_2O_3 agglomerates by CVD in a fluidized bed. *Mater Chem Phys* 1999;**59**:130–5.
14. Lin HT, Wang SC, Huang JL, Chang SY. Processing of hot pressed Al_2O_3–Cr_2O_3/Cr-carbide nanocomposite prepared by MOCVD in fluidized bed. *J Eur Ceram Soc* 2007;**27**:4759–65.
15. Lin HT, Liu BZ, Chen WH, Huang JL, Nayak PK. Study of color change and microstructure development of Al_2O_3-Cr_2O_3/Cr_3C_2 nanocomposites prepared by spark plasma sintering. *Ceram Int* 2011;**37**:2081–7.
16. Gong J, Peng Z, Miao H. Analysis of the nanoindentation load–displacement curves measured on high-purity fine-grained alumina. *J Eur Ceram Soc* 2005;**25**:649–54.
17. Zimmermann K, Schneider GA. Elastic to elastic–plastic transition of Al_2O_3/TiC ceramics studied by nanoindentation. *J Mater Res* 2009;**24**:1960–6.
18. Pharr GM, Oliver WC, Brotzen FR. On the generality of the relationship among contact stiffness, contact area, and elastic modulus during indentation. *J Mater Res* 1992;**7**:613–7.
19. Pharr GM, Oliver WC. An improved technique for determining hardness and elastic modulus using load and displacement sensing indentation experiments. *J Mater Res* 1992;**7**:1564–83.
20. Raveendran R, Pandya JR. Application of modified Kick's law in anisotropic studies of quenched potassium chloride cleavages. *Mater Chem Phys* 1996;**45**:1–5.
21. Gouldstone A, Chollacoop N, Dao M, Li J, Minor AM, Shen YL. Indentation across size scales and disciplines: recent developments in experimentation and modeling. *Acta Mater* 2007;**55**:4015–39.
22. Pezzotti G, Müller WH. Strengthening mechanisms in Al_2O_3/SiC nanocomposites. *Comput Mater Sci* 2001;**22**:155–68.
23. Choi SM, Awaji H. Nanocomposites – a new material design concept. *Sci Tech Adv Mater* 2005;**6**:2–10.
24. Awaji H, Choi SM, Yagi E. Mechanisms of toughening and strengthening in ceramic-based nanocomposites. *Mech Mater* 2002;**34**:411–22.
25. Paek YK, Lee HY, Kang S-JL. Direction of liquid film migration induced by chromic oxide in alumina–anorthite. *J Am Ceram Soc* 1996;**79**(12):3029–32.
26. Riu DH, Kong YM, Kim HE. Effect of Cr_2O_3 addition on microstructural evolution and mechanical properties of Al_2O_3. *J Eur Ceram Soc* 2000;**20**:1475–81.
27. Harabi A, Davies TJ. Densification and grain growth in sintered alumina–chromia powder mixtures. *Br Ceram Trans* 1995;**94**:97–102.
28. Li CL, Riu DH, Sekino T, Niihara K. Fabrication and mechanical properties of Al_2O_3 solid solution with low addition of Cr_2O_3. *Key Eng Mater* 1999;**161–163**:161–4.
29. Guicciardi S, Sciti D, Melandri C, Bellosi A. Nanoindentation characterization of submicro- and nano-sized liquid-phase-sintered SiC ceramics. *J Am Ceram Soc* 2004;**87**:2101.
30. McColm IJ. Ceramic Hardness. New York: Plenum Press; 1990.